Journal of Environmental Radioactivity 296 (2026) 107980

Contents lists available at ScienceDirect

Journal of Environmental Radioactivity

journal homepage: www.elsevier.com/locate/jenvrad

Radioactive (Pu, ^{210}Pb, ^{234}Th and ^{226}Ra) and chemical (Mn, Fe, Al) tracers to evaluate sediment accumulation and biodiffusion in the southern Gulf of Mexico

M. Díaz-Asencio [a,b,*], J.A. Corcho-Alvarado [c], O. Díaz-García [d], J.C. Herguera [b], M.A. Huerta-Diaz [e], P.T. Schwing [f], R. Larson [f], G.R. Brook [f], S. Röllin [c], L.W. Daessle [e]

[a] Escuela Nacional de Estudios Superiores Unidad Mérida, UNAM, Mérida, Yucatán, México
[b] Division of Oceanology. CICESE, Ensenada Center for Scientific Research and Higher Education, Ensenada, Baja California, México
[c] Nuclear Chemistry Division, Spiez Laboratory, Federal Office for Civil Protection, Spiez, Switzerland
[d] The Water Institute of the Gulf. Center for Coastal and Deltaic Solutions, Baton Rouge, LA, United States of America
[e] Instituto de Investigaciones Oceanológicas, Universidad Autónoma de Baja California, Campus Sauzal, Carretera Transpeninsular Ensenada-Tijuana, No. 3917, Frac. Playitas, Ensenada, Baja California, CP 22860, México
[f] Eckerd College, St. Petersburg, Florida, United States of America

ARTICLE INFO

Keywords:
Gulf of Mexico
Radionuclides
Sedimentation processes
Redox conditions
Deep-sea sediments

ABSTRACT

In this paper, we present results that have important implications for understanding the sedimentation process and for evaluating the carbon cycle in deep-sea sediment of the southern Gulf of Mexico (sGM) in the current context of global climate change.

Here we show results about short- and long-term biodiffusion rates obtained from natural (^{234}Th, ^{210}Pb, ^{214}Pb, ^{226}Ra) and anthropogenic ($^{239+240}$Pu) radionuclides in eleven sediment cores collected in the sGM: i) the outer continental shelf (2 cores), ii) the continental slope (5 cores), and iii) the abyssal plain (4 cores). The short- and long-term biodiffusion rates ($D_{b\text{-}Th}$ and $D_{b\text{-}Pb}$) ranged from 95 to 4135 cm^2 kyr^{-1} and 54 to 549 cm^2 kyr^{-1}, respectively.

The $D_{b\text{-}Th}$ (100 d time scale) values were less than one order of magnitude higher than the $D_{b\text{-}Pb}$ (100 yrs time scale), possibly because of the oligotrophic condition of the surface ocean in the sGM to limit the biological activity in sediments. Changes in redox conditions were confirmed by the enrichment of Fe and Mn in the sediment profiles.

These redox changes are likely responsible for increased Ra mobilization in the sediments and, consequently, for changes in the accumulation of unsupported ^{210}Pb. This process acts as an autochthonous source of $^{210}Pb_{ex}$ within the sediment layers and explains the disequilibrium observed between ^{214}Pb and ^{210}Pb in subsurface sections of some sediment cores.

Numerical simulation of $^{239+240}$Pu profiles using an advection-diffusion equation in non-steady-state conditions fit well ($R^2 > 0.86$) with measured $^{239+240}$Pu profiles in four of six cores. The biodiffusion rates obtained from the Pu model were comparable to those obtained from ^{210}Pb, but different than the short-term biodiffusion rates elucidated with ^{234}Th. The accumulation rates from Pu deconvolutions were similar to data reported previously by ^{14}C dating.

1. Introduction

Sediment accumulation and mixing rates are key parameters to understand biogeochemical processes in deep-sea sediments, and on their control of oxidation and preservation of organic carbon and sediment diagenesis (Díaz-Asencio et al., 2019; Lin et al., 2024; Smith and Rabouille, 2002a). Mixing rates, due to the bioturbation process, modify the physical, chemical, and biological properties of the sediments (Wetzel and Kohl, 1986; Yu et al., 2023), with significant effects on the structure and evolution of seafloor communities. These mixing processes

* Corresponding author. Escuela Nacional de Estudios Superiores Unidad Mérida, UNAM, Mérida, Yucatán, Mexico.
E-mail addresses: misaeldiazasencio1971@gmail.com, M.Diaz-Asencio@iaea.org (M. Díaz-Asencio).

https://doi.org/10.1016/j.jenvrad.2026.107980
Received 26 January 2026; Received in revised form 31 March 2026; Accepted 1 April 2026
Available online 24 April 2026

affect the upper centimeters, weakening the stratigraphic integrity of the high-resolution sedimentary record.

Accumulation of ^{234}Th and ^{210}Pb in deep-sea sediments have been used to estimate biodiffusion coefficients at different time scales (Nozaki et al., 1977; Pope et al., 1996). Since both radionuclides are very particle reactive, they are good tracers of particle transport and mixing. Their behavior in the ocean has been modeled using one-dimensional, steady-state diffusion models (Henderson et al., 1999). In these models, bioturbation is treated as analogous to molecular diffusion (Robbins et al., 1979) and is applied specifically to the fine sediment fraction, ranging from fine sand to silt.

Global fallout radionuclides (e.g., ^{137}Cs, ^{239}Pu, ^{240}Pu, and ^{241}Am) have also been used to evaluate mixing processes in deep-sea sediments (Legeleux et al., 1994; Roberts et al., 1997). These radionuclides were released during nuclear weapons testing (NWT), which began in the early 1950s and peaked in 1963. In abyssal sediments, mixing rates derived from NWT radionuclides have generally yielded higher values than those obtained from ^{210}Pb (Smith et al., 1993; Stordal et al., 1985). This has been explained by a preferential scavenging of the NWT radionuclides with the coarser and organic-rich particles, which are ingested and mixed at higher rates by animals (DeMaster and Cochran, 1982; Stordal et al., 1985).

Recent studies in the southern Gulf of Mexico (sGM) have focused on understanding sedimentation processes in deep-sea sediment. Díaz-Asencio et al. (2020), for example, used ^{210}Pb profiles from 15 cores to evaluate mixing processes in surface sediments (0 - 10 cm). The biodiffusion coefficients elucidated with the excess ^{210}Pb profiles ($D_{b\text{-}Pb}$), derived from advection-diffusion modelling, ranged from 14 to 51 cm^2 kyr^{-1} in the abyssal plain, and between 42 and 158 cm^2 kyr^{-1} in the continental slopes (Díaz-Asencio et al., 2020). The same study reported sediment accumulation in continental slopes and the abyssal plain of the sGM based on ^{14}C stratigraphies obtained from planktic foraminifera (using 42 sediment cores). In this study, a modified mixing box model (Erlenkeuser, 1980) was applied to evaluate the mean sedimentation rate (S_m) and to estimate the age of surface sediments (T_0) that result from mixing processes (Carvalho et al., 2011; Kershaw, 1985). The S_m ranged between 5 and 9 cm kyr^{-1} in cores from the abyssal plain and continental slopes, with highest values consistently observed in specific locations of the slopes (17 - 24 cm kyr^{-1}).

In another study in the sGM, Corcho-Alvarado et al. (2022) used $^{239+240}$Pu profiles obtained from six deep-sea sediment cores to evaluate $^{239+240}$Pu sources and its transport from the ocean surface to the seafloor. This study found that $^{239+240}$Pu in deep-sea sediments originated from two different sources: i) regional fallout from the Nevada Testing Site (NTS), and ii) global stratospheric fallout from the Nuclear Weapons Tests (NWTs). The distinct ^{240}Pu/^{239}Pu isotopic ratios of these two sources were used to determine the relative contribution of each source to the total $^{239+240}$Pu in the sediments. The contribution of the NTS steadily increased in depth, accounting for over 45% in the abyssal region.

The oligotrophic conditions of the surface waters in the sGM produce a low export of organic carbon to the deep-sea sediments, especially to the abyssal plain, and sustain a trophic benthic structure with a higher proportion of micro and meiofauna than macrofauna (Díaz-Asencio et al., 2020). Under these conditions, organic matter remineralization ceases at depths where oxygen is still available, but organic carbon concentrations have declined, and the redox boundaries are typically located several decimeters beneath the sediment–water interface (Sarmiento and Gruber, 2005). These processes affect the distribution of several redox-sensitive elements like Mn and Fe. Layers enriched in Mn and Fe can act as traps for ^{226}Ra (and its radioactive decay daughter products), which would explain the higher supported ^{210}Pb observed in some sediment profiles in the abyssal zones (Suckow et al., 2001; Watson and Angino, 1969).

In this study, we estimate the sediment accumulation and biodiffusion coefficients rates from the vertical distribution of four radionuclides (^{14}C, ^{234}Th, ^{210}Pb and ^{239,240}Pu) in 11 sediment cores collected in the sGM. Using an advection-diffusion model, assuming steady-state conditions, we estimate the short- and long-term mixing parameters using ^{234}Th and ^{210}Pb depth profiles, respectively. Furthermore, applying a numerical solution of the advection-diffusion model, in non-steady-state condition and assuming a pulse of plutonium at the seafloor in 1960, we simulate Pu profiles in deep-sea sediments by tuning the biodiffusion and sedimentation parameters. These parameters are compared with those obtained by other approaches, such as biodiffusion rates calculated from ^{234}Th and ^{210}Pb profiles and sediment accumulation rates estimated using ^{14}C in planktic foraminifera (Díaz-Asencio et al., 2023). In our approach, the biodiffusion terms include both molecular diffusion and biodiffusion associated with bioturbation processes. Finally, the depth profiles of Al-normalized Mn and Fe in the sediment cores are used to identify the redox boundaries and evaluate their effect on supported ^{210}Pb.

2. Materials and methods

2.1. Study area

The Gulf of Mexico is a critical passageway for a major western boundary current in the North Atlantic, transporting water, salt, oxygen, matter, and energy from the tropics to the Atlantic Ocean as part of the Meridional Overturning Circulation. Tropical surface, intermediate, and deep waters flow from the Caribbean into the Gulf of Mexico through the Yucatán Channel, forming the Loop Current; its outflow through the Florida Straits feeds into the Gulf Stream, carrying water, salt, and energy toward the high-latitude North Atlantic (Athié et al., 2015, 2020; Sheinbaum et al., 2016; Sturges et al., 2010). Over timescales of several months to years the Loop Current sheds large eddies—up to 200 km in radius and 1000 m deep—into the interior of the Gulf. These eddies contribute a significant volume of Caribbean water and play a key role in controlling basin circulation from the surface to the deepest layers, while also supplying salt, oxygen, carbon, and nutrients to the interior (Leben, 2013; Meunier et al., 2018, 2020; Quintanilla et al., 2024). Water masses above ~700 m exit through the Florida Straits, whereas deeper waters return to the Caribbean basins (Sheinbaum et al., 2016). These circulation processes, combined with their status as a semi-enclosed tropical marine basin, generate particular biogeochemical and ecological conditions in the water column and sediments, from coastal zones to abyssal depths.

The southern Gulf of Mexico is surrounded by the Sigsbee Abyssal Plain to the north, the Yucatan Platform to the east, the Campeche Slope to the southwest and the Mexican Ridges to the west (Fig. 1). The Yucatan Platform is predominantly carbonate and contributes very little siliciclastic sediments to this region (Holmes, 1976). Siliciclastic sediment input is primarily associated with major river systems including: i) Mississippi-Atchafalaya system to the north, ii) the Eastern Sierra Madre rivers to the west, and iii) the Grijalva-Usumacinta river complex to the south.

2.2. Sampling and sample processing

This study is based on 11 sediment box cores collected in 2017 aboard the BO/Justo Sierra, during the oceanographic cruise XIXIMI-7 (Fig. 1). Sediment cores were collected from the outer continental shelf (B8E21 and B8E36), the continental slope (TS1, B11, E33, F38 and B18), and the abyssal plain of the sGM (C22, C23, D29, A10). The core lengths varied between 15 and 25 cm. Sediment were retrieved with a Soutar box corer (40 × 40 cm) and subsampled on board, using acrylic tubes (inner diameter of 8.0 cm) and kept at 4 °C during transport to the laboratory. The cores were split lengthwise, photographed, and one of the half sections was sampled at a high resolution (2 mm). Pretreatment of sediment cores in the laboratory was executed immediately to measure short-lived radioisotopes and avoid geochemical changes in the

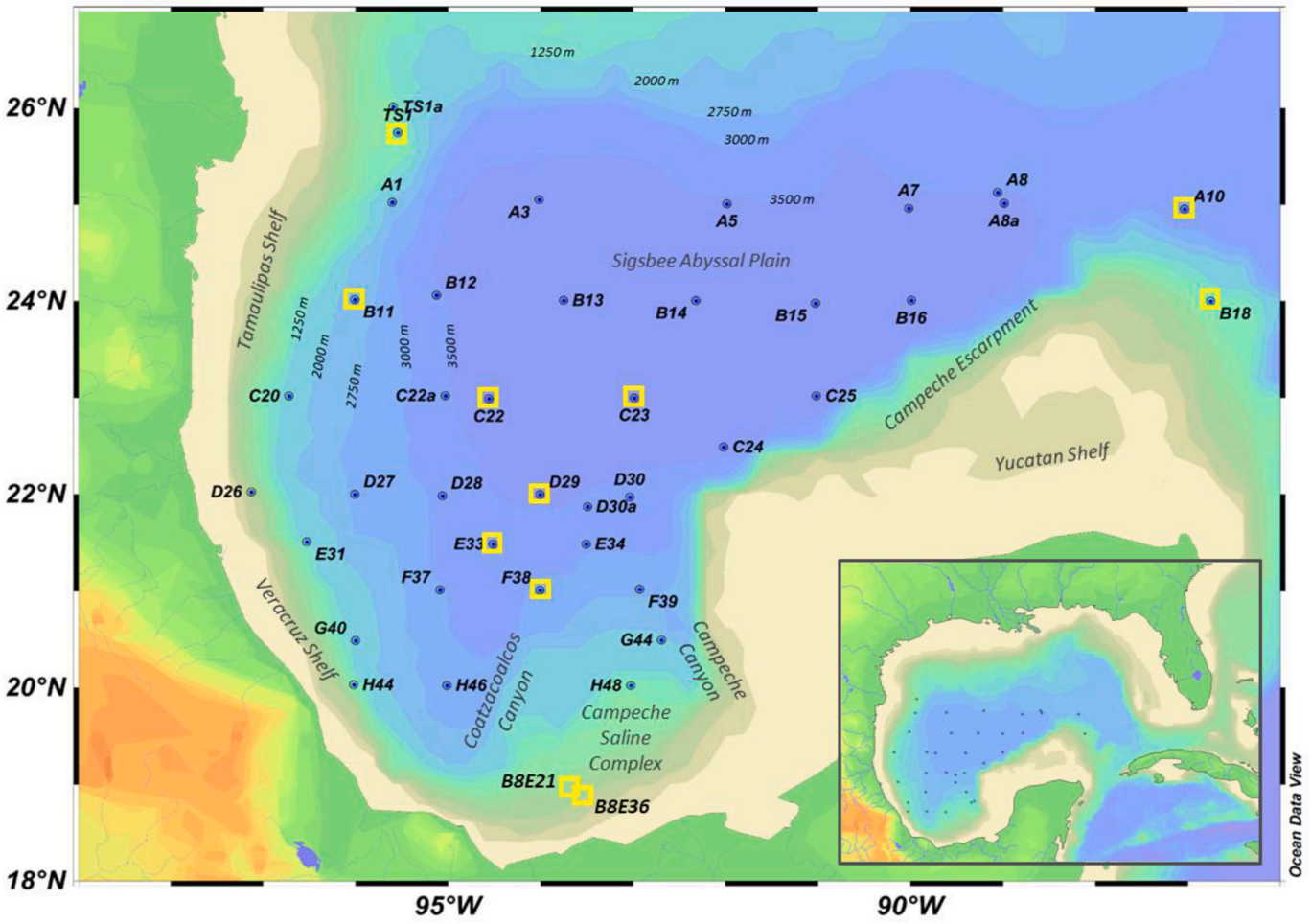

Fig. 1. Sampling stations of sediment cores collected in the continental slopes and abyssal region of the southern Gulf of Mexico during the cruises XIXIMI (I to VII). The yellow squares are the cores recovered during the cruise XIXIMI-VII (from May to September 2019), used in this study. Sediment cores B8E21 and B8E36 at the end of the south continental shelf, were collected in March 2018. (For interpretation of the references to color in this figure legend, the reader is referred to the Web version of this article.)

sediment cores. The sediment samples were freeze-dried and ground to very fine powder in agate mortars.

2.3. Laboratory analysis

Aliquots were taken from each sediment layer and analyzed by high-resolution gamma-ray spectrometry using high-purity germanium (HPGe) detectors. Sediment samples were analyzed following the methods used by Díaz-Asencio et al. (2020), Larson et al. (2018a) and Schwing et al. (2017). The total activities of ^{210}Pb (46.5 keV), ^{234}Th (63 keV), ^{214}Pb (295 keV and 351 keV) and ^{214}Bi (609 keV) were analyzed in HPGe coaxial planar detectors. Efficiency calibrations of the HPGe detectors were based on the analysis of the certified reference materials IAEA-447 (Moss-Soil, IAEA, Austria) and DL1a (Uranium-Thorium Ore, Canada Centre for Mineral and Energy Technology, Canada). Sediment samples were analyzed at the University of South Florida (US), Eckerd College (US) and the Oceanological Research Institute (Autonomous University of Baja California, Mexico). ^{226}Ra was determined from its daughter nuclides, ^{214}Pb and ^{214}Bi, assuming that secular radioactive equilibrium between ^{226}Ra and ^{222}Rn was achieved after three weeks storage in sealed containers. Excess ^{210}Pb (^{210}Pb$_{ex}$) in each sample was calculated as the difference between the total ^{210}Pb and the supported ^{210}Pb, the latter derived from the ^{226}Ra (^{214}Pb-^{214}Bi) activity.

Due to its short half-life (24.1 d), ^{234}Th activity decreases rapidly with depth in all cores. The supported ^{234}Th (from its parent ^{238}U) in each core was determined in the depth at which the ^{234}Th profile exhibited a constant value. Excess ^{234}Th was calculated as the difference between the total and supported activities in the sediment sections. In all cases, the excess ^{234}Th was corrected for the decay between the time of sampling and sample analysis (Brooks et al., 2015b; Larson et al., 2018b).

Additionally, we estimated the ^{226}Ra concentration in selected cores using its gamma peak at 186.2 keV. Although this line is not recommended for quantitative analysis due to interference from the ^{235}U peak at 185.7 keV, it can be used to identify significant qualitative changes in ^{226}Ra activities.

Total concentrations of Fe, Al and Mn were measured using portable X-ray fluorescence equipment (pXRF; model DELTA Premium), with its software in geochemical mode. Dry and homogenized samples were used to reduce interferences. The dry, fine-ground sample was placed in a Chemplex® 1900 plastic container whose lower orifice was covered with a circular Mylar® polyester film 3.6 μm uniform thickness. Calibration of the pXRF and measurement of the samples were conducted following the procedure described by Mejía-Piña et al. (2016), using 33 certified reference materials and internal standards. Each analysis was performed with a total exposure time of 360 s and a sample thickness of ≥0.5 cm within the container.

Pu radioisotopes were analyzed in six sediment cores (B8E36, B8E21, TS1, F38, C23, A10), as described elsewhere (Corcho-Alvarado et al., 2022; Röllin et al., 2009; Sahli et al., 2017). Briefly, Pu radioisotopes

were separated and purified in a TEVA resin and then analyzed with a sector field inductively coupled plasma mass spectrometer (SF-ICP-MS) model Element XR (Thermo Fischer Scientific). An Apex nebulizing system connected to an ACM desolvator and a self-aspirating PFA-ST--nebuliser (all from Elemental Scientific Incorporation, USA) were used for introducing the samples into the system. Pu isotope concentrations were calculated from the signal of the ^{242}Pu tracer. The contributions from the tracer and tailing from U and Th on the Pu signal were corrected mathematically based on the isotope ratios from the certificate and abundance sensitivity measurements of U and Th standards.

2.4. Radionuclides as tracers of transport modelling in sediments

The mass balance equation for a particulate constituent *B*, which is part of the solid particles in the sediments, can be expressed as (Sarmiento and Gruber, 2005):

$$\frac{\partial(1-\varnothing)\cdot B}{\partial t} = -ADV\,(B) + DIFF\,(B) + SMS\,(B) \quad (1)$$

in this general case, *B* is the concentration (mol·m^{-3}) and ∅ is porosity. The terms *ADV (B)* and *DIFF (B)* represent the advection and biodiffusion processes; and *SMS (B)* represents the loss of *B* due to different processes/effects. This general equation can be applied to describe the transport of a radionuclide *B* in sediment cores as (Officer, 1982; Officer and Lynch, 1983):

$$\frac{\partial B}{\partial t} = -S_m\frac{\partial B}{\partial z} + D_b\frac{\partial^2 B}{\partial z^2} - \lambda_B\cdot B \quad (2)$$

where *B* is now the activity concentration of the radionuclide in question (in Bq·kg^{-1}), *t* is time, *z* is depth in the sediment profile (increasing downward), λ_B is the radioactive decay constant of *B*, and D_b is the mean particle biodiffusion coefficient by bioturbation (cm^2·kyr^{-1}). It is assumed that sediment mixing by bioturbation is analogous to diffusion over the timescale of interest provided by the radionuclide. Finally, S_m is the mean sedimentation rate (cm·kyr^{-1}), calculated from ^{14}C-dated planktic foraminifera in sediments below the homogenous mixed layer (Fig. 2). The values of S_m in the 11 cores were reported elsewhere (Díaz-Asencio et al., 2023).

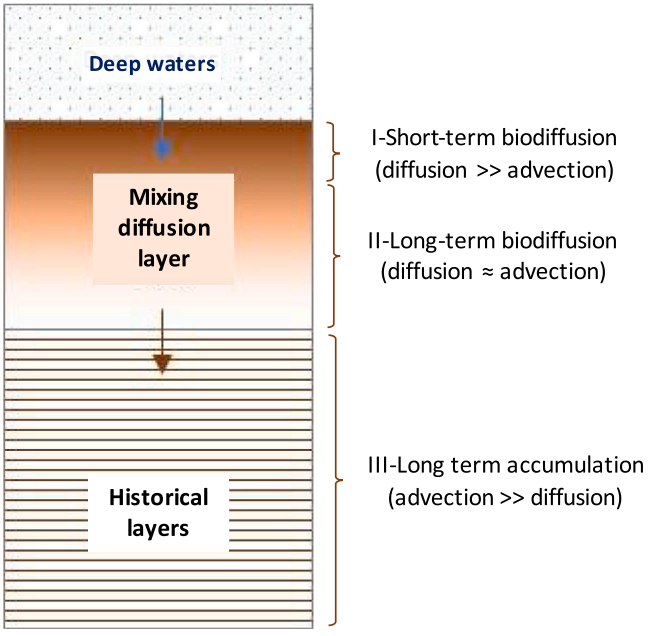

Fig. 2. Representation of the sedimentation accumulation processes in marine bottom depth. Biodiffusion processes dominate the surface mixing layer (below the water-sediment interface); for this evaluation, we divided it into short- and long-term biodiffusion coefficients calculated by the profiles on ^{234}Th and ^{210}Pb, respectively. Below the surface mixing layers, the historical record layers are characterized by predominated sediment accumulation and minimal mixing. Accumulation patterns in this layer are estimated using ^{14}C dating.

The porosity (∅) was calculated as:

$$\varnothing = 1 - \frac{DBD\,(z)}{DSD} \quad (3)$$

in our study a Dry Solid Density (DSD) of 2.62 g cm^{-3}, corresponds to the particle density, is assumed similar for sediments from slopes and abyssal zones of the sGM. The Dry Bulk Density (DBD, in g·cm^{-3}) was calculated as the dry mass of each sediment section divided by its bulk volume (Brooks et al., 2015a).

For ^{210}Pb and ^{234}Th, equation (2) is applied under steady-state conditions ($\partial B/\partial t = 0$; as it is assumed that the fluxes of ^{210}Pb and ^{234}Th to the sediment-water interface remain constant with time). For both radionuclides, biodiffusional mixing competes with radioactive decay to generate an exponential decrease of activity with increasing depth (Anderson et al., 1988; Guinasso and Schink, 1975; Koide et al., 1972; Robbins, 1978). Due to the short half-life of ^{234}Th, the solution of equation (2) will report mean biodiffusion processes in short time scales (last few months and first mm in sediment core). At this scale, mixing is more important than accumulation and the advection term equal 0 (see Fig. 2). Equation (2) can then be simplified as:

$$D_{b1}\frac{\partial^2 B}{\partial z^2} - \lambda_B\cdot B = 0 \quad (4)$$

where B is the excess activity of ^{234}Th in the sediment profile, *z* is depth in the sediment profile, and D_{b1} represents the average biodiffusion coefficient for the biologically mixed layer I (surface mixing layer), where the remineralization of particulate organic matter by benthic communities is more rapid and higher than in deeper sections (Alperin et al., 2002).

In this case, applying the linear fit to the ^{234}Th$_{ex}$ profiles using equation (5) allows estimation of $D_{b\text{-}Th}$ in short-term and the mixing depth ($X_{ML\text{-}Th}$) of mixed layer I. In this case, $X_{ML\text{-}Th}$ represents the maximum sediment depth to which excess ^{234}Th can penetrate

$$\ln\frac{^{234}Th_{ex}\,(z)}{^{234}Th_{ex}\,(z=0)} = -Z\sqrt{\frac{\lambda_{Th234}}{D_{b1}}} \quad (5)$$

For ^{210}Pb, the solution of equation (2) provides average biodiffusion processes in long-term scales (decades to up 100 yrs), with values of biodiffusion coefficients that are expected to be orders of magnitude lower than those based on excess ^{234}Th (Smith et al., 1993). Hence, for ^{210}Pb, equation (2) takes the following form:

$$D_{b2}\frac{\partial^2 B}{\partial z^2} - S_m\frac{\partial B}{\partial z} - \lambda_B\cdot B = 0 \quad (6)$$

where B is the excess ^{210}Pb activity in the sediments and D_{b2} ($D_{b\text{-}Pb}$) represent the average biodiffusion coefficient for the mixed layer II (deep mixing layer), where the particulate organic matter is less labile and therefore the rate of remineralization is slower (Alperin et al., 2002). On this time scale, both processes (mixing and advection) are responsible for the vertical transport of particulate matter in sediments.

Considering the boundary conditions: i) $B=B_0$ at $z = 0$, and ii) $B \to 0$, as $z \to \infty$. The analytical solution for Eq. (6) is:

$$\ln\frac{^{210}Pb_{ex}\,(z)}{^{210}Pb_{ex}\,(z=0)} = \frac{S_m - \sqrt{{S_m}^2 + 4\,\lambda_{Pb210}\,D_{b2}}}{2D_{b2}}z \quad (7)$$

Officer (1982) estimated the average biodiffusion coefficient ($D_{b\text{-}Pb}$) from equation (7) using the apparent sedimentation rate (S_m') from the ^{210}Pb$_{ex}$ profile and the mean sedimentation rate S_m (calculated from ^{14}C age-depth profiles) through the expression:

$$D_{b-Pb} = \frac{(S_m' - S_m)}{\lambda_{Pb_{210}}} \quad (8)$$

To solve equation (8), we used S_m reported elsewhere for each sediment core below the homogenous mixed layer (Díaz-Asencio et al., 2023).

The total unsupported ^{210}Pb inventory (Bq·m^{-2}) in each core is the sum of excess ^{210}Pb accumulated in all sediment layers (equation (9)). The excess ^{210}Pb accumulated in each layer is calculated by multiplying the dry bulk density (g·cm^{-3}) of the interval by the activity (Bq·kg^{-1}) and the thickness of the interval (cm) (Appleby and Oldfield, 1978; Robbins, 1978). Furthermore, the total flux (Bq·m^{-2}·yr^{-1}) can then be estimated by multiplying the total inventory (Bq·m^{-2}) by the decay constant of ^{210}Pb (yr^{-1}).

$$Total\ Inventory\ ^{210}Pb_{ex} = \sum_{i=1}^{n} DBD_{(i)} \cdot {}^{210}Pb_{ex\ (i)} \cdot L_{(i)} \quad (9)$$

On the other hand, the flux of ^{210}Pb$_{ex}$ from the water column to the sediment-water interface was calculated from equation (10), based on the mean DBD, the apparent sedimentation rate (S_m') from the ^{210}Pb$_{ex}$ profile and the ^{210}Pb$_{ex}$ (0) activity in the water-sediment interface.

$$Flux^{210}Pb_{ex} = S_m' \cdot DBD \cdot {}^{210}Pb_{ex}(0) \quad (10a)$$

For Pu radioisotopes, given their long half-lives, the radioactive decay term in equation (2) is neglected. The model is applied in non-steady-state conditions given the relatively recent introduction of Pu into the environment. The model assumes that the Pu input (Nevada fallout and global fallout) arrived to the deep-sea sediments as a pulse in 1960. This assumption is based on previous studies that concluded that the bulk of Pu in deep sediments in the North Atlantic (depths >1200 m) arrived shortly after the peak depositional years of both Nevada and global fallout sources (Buesseler and Sholkovitz, 1987a, 1987b). These studies also demonstrated that altering the year of either the Nevada or global fallout input to the deep-sea sediments by two to six years did not alter appreciably the profiles which were generated by the advective-diffusive model. The magnitude of the Pu pulse for each sediment core was estimated from the inventory of Pu in each core (Alperin et al., 2002; Corcho-Alvarado et al., 2022). In this case, equation (2) can be presented as:

$$\frac{\partial^{239+240}Pu\ (t)}{\partial t} = -S_m \frac{\partial^{239+240}Pu\ (z)}{\partial z} + D_b \frac{\partial^2\ {}^{239+240}Pu\ (z)}{\partial z^2} \quad (10b)$$

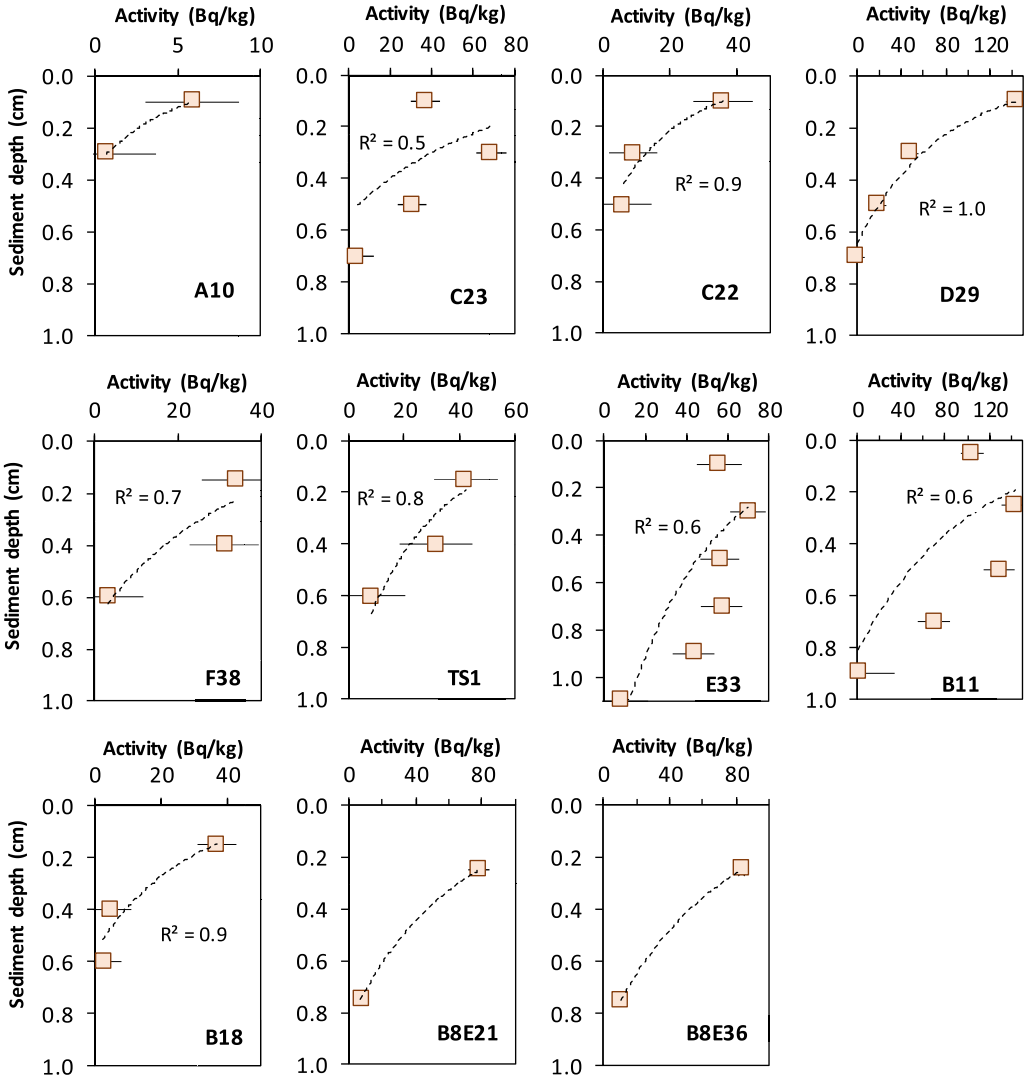

Fig. 3. Excess ^{234}Th activity profiles in 11 sediment cores from the southern Gulf of Mexico (sGM), each accompanied by its corresponding exponential fit (dashed line). The horizontal bars represent the uncertainties estimated at a 68% confidence level.

A finite differential method was applied to solve equation (10) for the six sediment cores Pu analyzed, assuming a pulse of Pu into the sediments in 1960. We assume that surface and deep mixed layers evaluate short- and long-term biodiffusion processes, respectively (Alperin et al., 2002; Benninger et al., 1979). Consequently, we derived a set of short- and long-term biodiffusion coefficients (D_{b1} and D_{b2}, respectively) and compared them with $D_{b\text{-}Th}$ and $D_{b\text{-}Pb}$, respectively, calculated from the ^{234}Th and ^{210}Pb profiles. The sediment accumulation rates (S_m") derived from Pu simulation for each core were also compared with the values previously reported by Díaz-Asencio et al. (2023) based on ^{14}C AMS ages.

3. Results

3.1. Biodiffusion coefficient inferred from ^{234}Th data

In most sediment cores (8 of 11), the excess of ^{234}Th profiles fit well ($R^2 > 0.6$) to a negative exponential model (Fig. 3), while three cores (C23, E33, B11) showed large surface mixing layers, suggesting non-diffusive mixing on ^{234}Th timescales (~100 days). Excess ^{234}Th at the surface exceeded 40 Bq kg^{-1} in all but core A10 (6 Bq·kg^{-1}). Using equation (5), we calculated the mean biodiffusion coefficient ($D_{b\text{-}Th}$) and the mixing depth ($X_{ML\text{-}Th}$) in the sediment mixed layer I (it represents circa 100 d of time) for all cores (Table 1). $D_{b\text{-}Th}$ and $X_{ML\text{-}Th}$ were generally low (<0.83 cm^2 yr^{-1} and <1.3 cm), except for E33, and showed no trend with seafloor depth; A10 displayed negligible mixing.

3.2. ^{210}Pb and ^{214}Pb depth profiles and change in sediment composition

In core A10 (Fig. 4 I), a distinct change in sediment composition is evident, marked by a decrease in $CaCO_3$ concentration (from around 50 % in the top to lower than 5 % below 15 cm) and corresponding increases in Al and Fe toward the bottom of the core. Concentration data from Al, Fe, and Mn in all sediment cores have been shown in the supplementary material (Table S1). In this core, the Mn/Al and Fe/Al molar ratios remain constant with depth (profiles not shown due to space constraints). This pattern is generally observed in sediments affected by carbonate dissolution (e.g., Sarmiento and Gruber, 2005).

In all cores from the continental slope and the abyssal plain ^{210}Pb and ^{214}Pb profiles reveal an initial exponential decrease of ^{210}Pb in surface layers, followed by intermediate-depth enrichment (6-15 cm) in several cores (e.g., A10, C23, D29, F38, TS1, B11), coinciding with increased ^{214}Pb and ^{226}Ra at depth (Fig. 4 I and 4 II). In these cores the ^{210}Pb at the surface exceeded 1000 Bq·kg^{-1}, with a highest value of 2788 Bq·kg^{-1}, in the core B11. Peaks in Mn/Al or Fe/Al ratios and dark sediment bands mark redox transitions, often associated with suboxic conditions.

The outer shelf cores exhibit a regular exponential decline for ^{210}Pb (not intermediate-depth enrichment) but show distinct Mn/Al and Fe/Al maxima near the surface. In core B8E21, the Mn/Al ratio was maximum and constant in the first 2.5 cm, and the Fe/Al increases slightly toward the surface of the core, where the sediments show lighter colors. However, in core B8E36, the Mn/Al and Fe/Al ratios showed maximum at 1 cm and 2 cm, respectively, marking the limit of the oxic layer. These high Mn/Al and Fe/Al ratios, near the core top, could be due to another process that is not seen in the rest of the cores.

Regarding the ^{226}Ra estimated profiles in sediments, in the four cores evaluated (A10, C23, F38 and TS1) we observed an increase in ^{226}Ra (counts per gram) in sediment layers, with peaks coinciding with maxima in the Mn/Al ratio at the oxic layer boundary. The mobility of Ra, and thus the isotope ^{226}Ra, in aquatic sediments is largely governed by redox reactions and adsorption processes (Mangeret et al., 2020). In deeper sediment layers characterized by suboxic conditions, Fe and Mn oxyhydroxides are reductively dissolved (Froelich et al., 1979), resulting in the release of ^{226}Ra previously associated with these mineral phases. As dissolved Fe and Mn diffuse upward into the oxic sediment zone, they reprecipitate, thereby scavenging ^{226}Ra (Kirk Cochran and Kadko, 2008).

Consequently, this redox cycle leads to a net upward diffusive flux of ^{222}Rn. Among its decayed products, ^{210}Pb, owing to its relatively long half-life, is the most affected by this diagenetic process. This process enhances excess ^{210}Pb in intermediate and surface layers, a mechanism previously noted in Pacific Ocean (Suckow et al., 2001) and the Gulf of Mexico (Díaz-Asencio et al., 2020; Watson and Angino, 1969) sediments but rarely explained in earlier studies.

3.3. ^{210}Pb in excess to evaluate biodiffusion coefficient and recent diagenesis

Fig. 5 presents the vertical profiles of excess ^{210}Pb (expressed as ln $^{210}Pb_{ex}$) for the eleven sediment cores. In the upper 3–10 cm of all cores, the data exhibit a reasonably strong fit ($R^2 > 0.7$) to a negative linear regression, reflecting control by the flux of $^{210}Pb_{ex}$ from the water column to the sediment-water interface. However, an "excess" of ^{210}Pb was also observed in deeper layers of the cores (from abyssal and continental slopes), probably associated with sources other than the ^{210}Pb flux from the water column. As hypothesized in this work, the accumulation of ^{226}Ra in the oxic boundaries of the core probably generates an upward diffusion of ^{222}Rn into the upper layers, increasing in the process the ^{210}Pb in excess.

In cores E33, B11, B18, B8E21, and B8E36 (Fig. 5), the gray horizontal bar marks the transition from oxic to suboxic conditions. In the remaining cores, this boundary occurs deeper, typically below 16 cm.

Table 1
Results derived from the $^{234}Th_{ex}$ and $^{210}Pb_{ex}$ biodiffusion models in the sediment cores from the southern Gulf of Mexico, with the uncertainties estimated (u) at a 68% confidence level.

Region	Station	Water Depth m	$X_{ML\text{-}Th}$ cm		$D_{b\text{-}Th}$ cm^2·kyr^{-1}		Flux $^{234}Th_{ex}$ Bq·m^{-2}·yr^{-1}		$X_{ML\text{-}Pb}$ cm		$D_{b\text{-}Pb}$ cm^2·yr^{-1}		Flux $^{210}Pb_{ex}$ [a] Bq·m^{-2}·yr^{-1}		Flux $^{210}Pb_{ex}$ [b] Bq·m^{-2}·yr^{-1}
			mean	u	mean	u	mean	u	mean	u	mean	u	mean	u	mean
Cont. shelf	B8E36	257	1.3	0.0[c]	628	0[c]	2095	62	33	6	549	207	505	91	506
Cont. shelf	B8E21	419	1.1	0.0[c]	443	0[c]	2252	207	18	3	206	32	325	56	277
Cont. slope	XI7-TS1	2417	1.3	0.6	832	370	670	141	18	4	159	62	399	95	523
Cont. slope	X17-B11	2400	1.3	0.7	487	260	2886	615	18	4	150	32	561	115	632
Cont. slope	XI7-E33	3435	2.9	1.4	4135	1899	1132	185	5	2	8	3	113	41	330
Cont. slope	XI7-F38	2822	0.9	0.6	418	259	396	148	17	2	164	27	277	40	322
Cont. slope	X17-B18	1182	0.7	0.2	276	60	472	163	8	2	36	12	138	41	248
Abyssal plain	XI7-C23	3739	1.3	0.8	810	456	671	132	11	4	77	54	105	41	196
Abyssal plain	XI7-A10	3340	0.3	0.0[c]	95	0[c]	96	63	9	2	54	17	133	22	193
Abyssal plain	XI7-C22	3729	0.9	0.3	539	117	213	119	9	3	72	32	53	12	243
Abyssal plain	X17-D29	3564	1.1	0.1	425	24	823	183	12	3	85	42	185	50	288

[a] Fluxes of the ^{210}Pb in excess from the water-sediment interface (calculated using equation (10)).
[b] Fluxes of the ^{210}Pb in excess estimated from the total inventory in the sediment core (multiplying the total inventory by the decay constant of ^{210}Pb (yr^{-1}).
[c] Values with uncertainties = 0 were obtained by a linear regression of two points only.

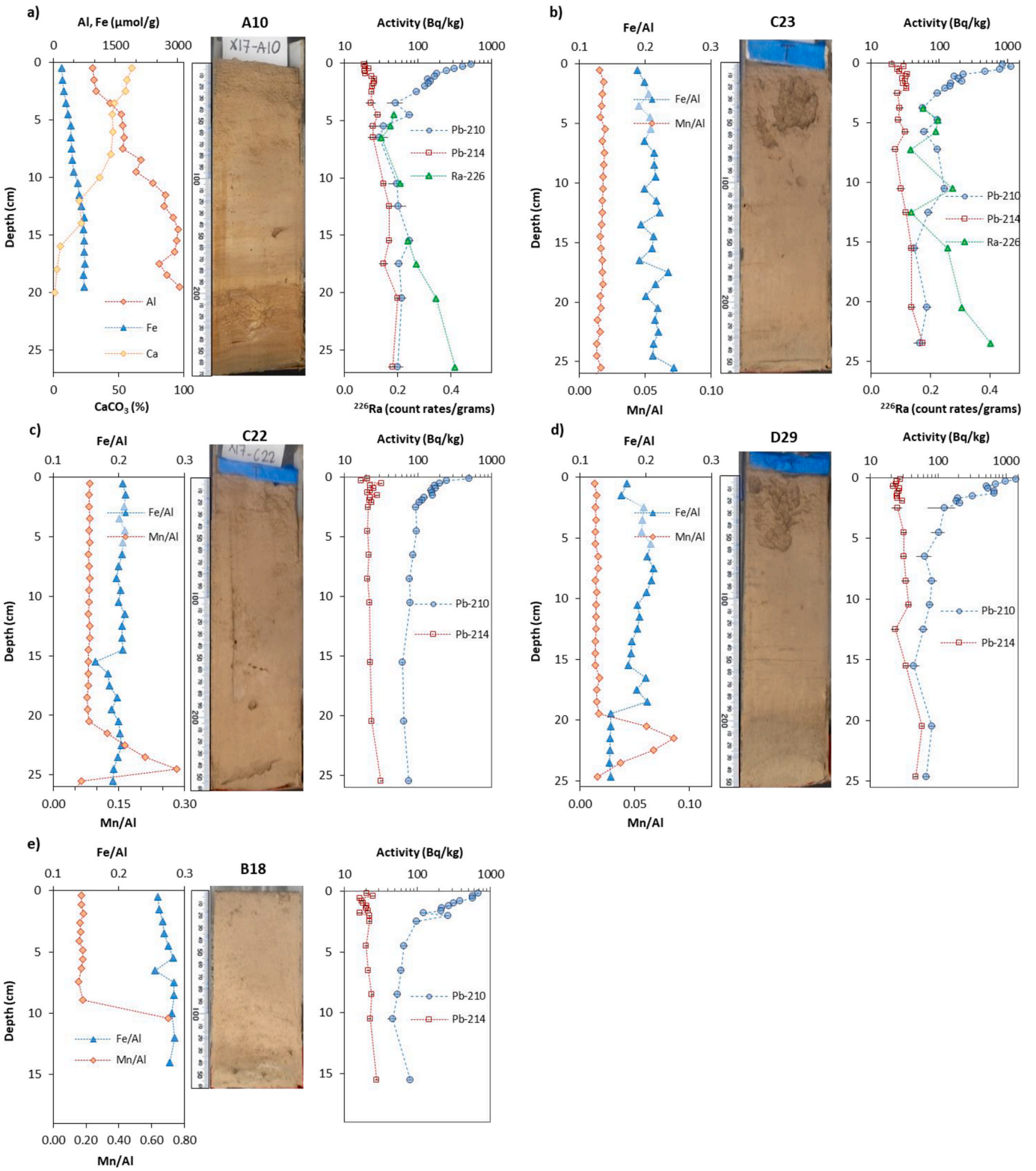

Fig. 4. Depth profiles of gamma-emitter activities (^{210}Pb and ^{214}Pb), counts per gram (^{226}Ra at 186 keV), and elemental ratios (mol/mol) of Fe/Al and Mn/Al in all sediment cores. Included are the photographs of the vertical sections of each sediment core, highlighting their internal structure and stratigraphy. I) Data information from the abyssal zone stations a) A10, b) C23, c) C22, d) D29, and e) B18. II) Data information from the continental slopes f) F38, g) TS1, h) B11, i) E33 and continental shelf j) B8E21, k) B8E36 stations. The horizontal bars represent the uncertainties estimated at a 68% confidence level.

Applying a linear fit to the top section of each core (Fig. 5) and using equation (8), we calculated the mean biodiffusion coefficient ($D_{b\text{-}Pb}$) and the mixing depth ($X_{ML\text{-}Pb}$) in the biodiffusion mixing layer (representing about 120 yrs in time). The results for each core are resumed in Table 1. The $X_{ML\text{-}Pb}$ ranged from 5 to 18 cm in cores from the slope and abyssal zones, and from 18 to 33 cm in cores from the continental shelf. In cores

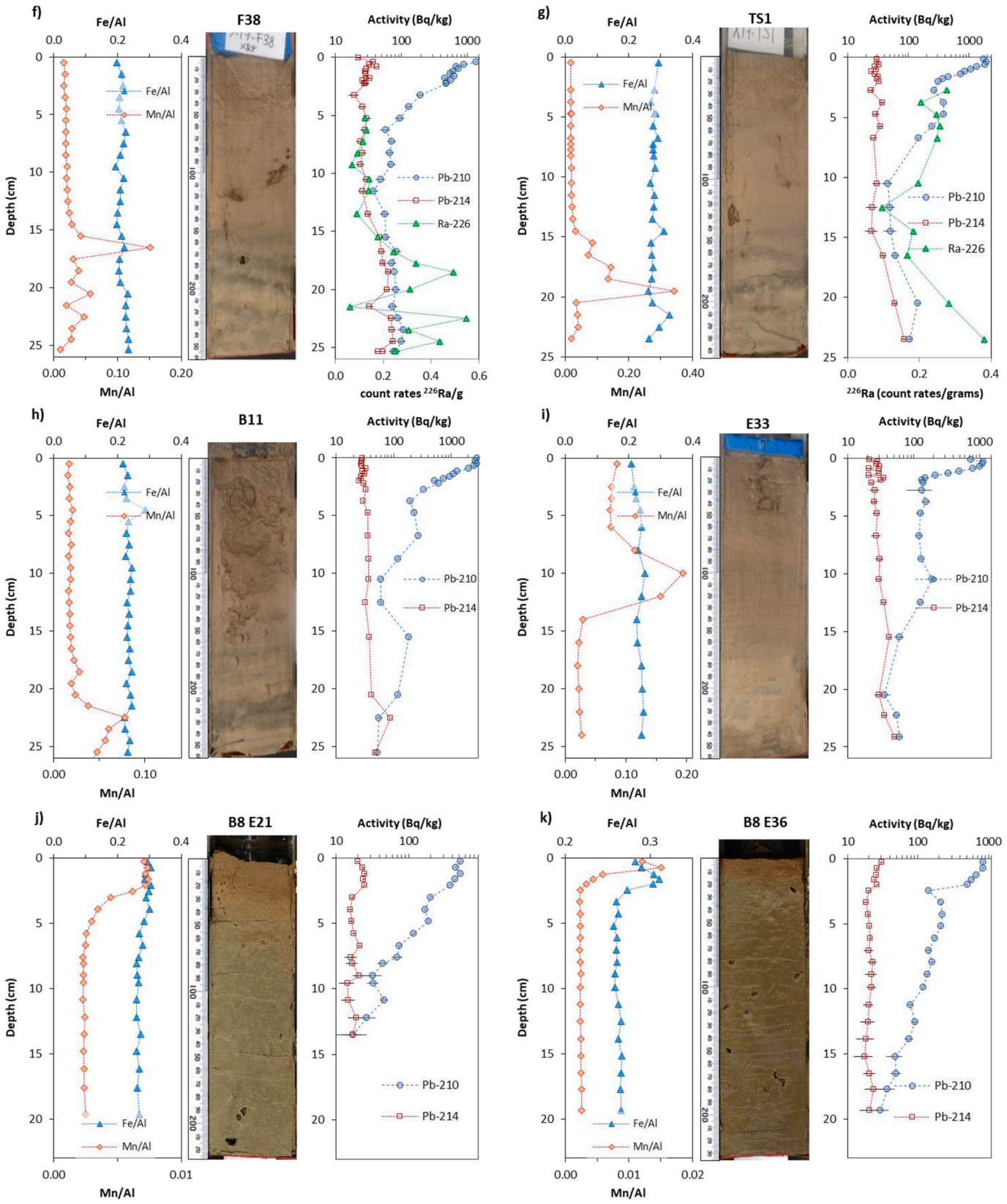

Fig. 4. (*continued*).

from the slopes and abyssal regions, the $D_{b\text{-}Pb}$ ranged from 8 to 159 cm^2 yr^{-1}. Higher biodiffusion coefficients (206 and 549 cm^2 yr^{-1}) were obtained for cores B8E21 and B8E36 from the continental shelf, respectively. The lowest mixing was observed in core E33, where the boundary of oxic to suboxic conditions occurs at 10 cm depth (very shallow), probably limiting the biological activity below that depth.

Using the best fit parameters to the measured data, we estimated the ^{210}Pb fluxes from the water column to the water-sediment interface,

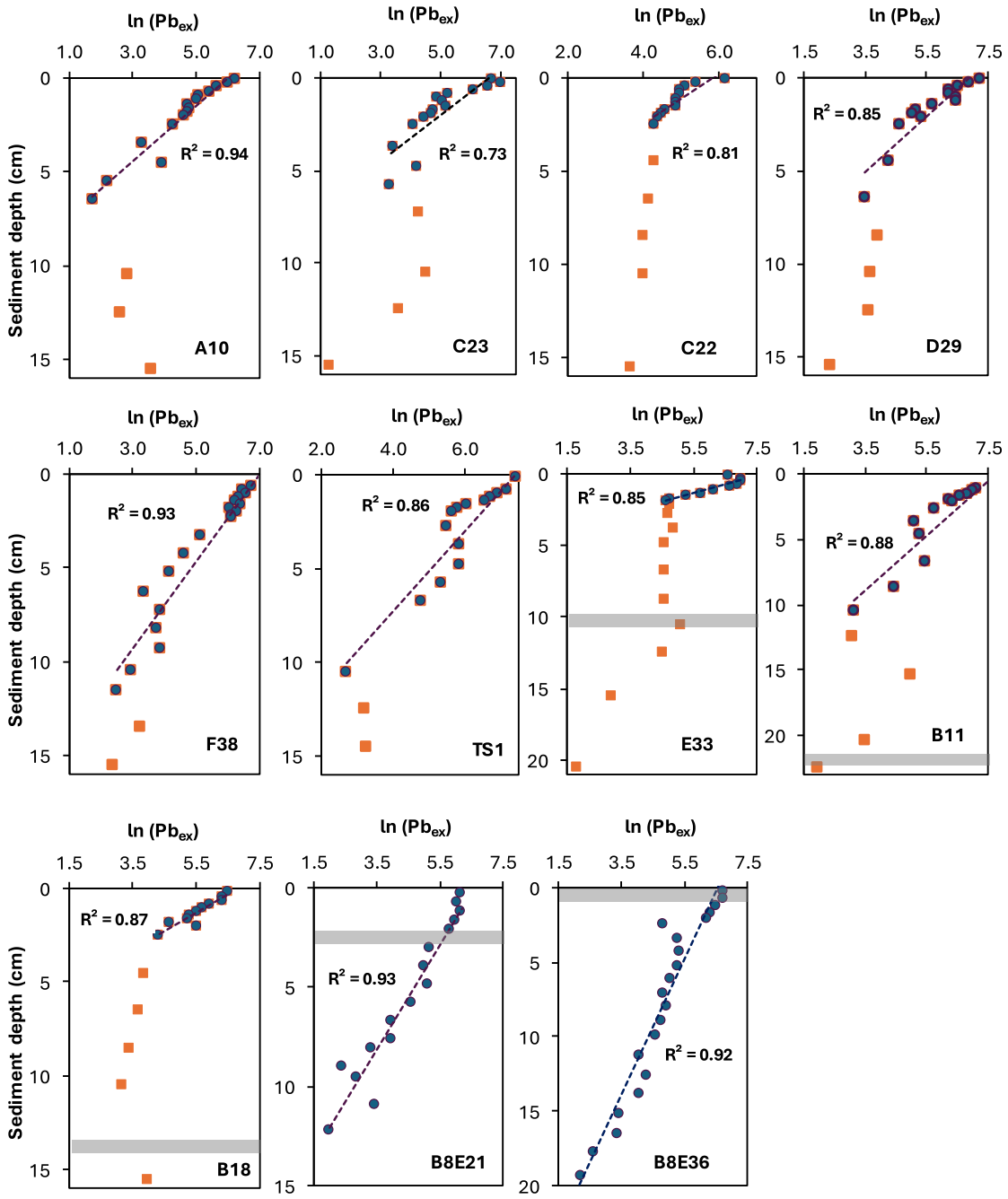

Fig. 5. Depth profiles of the ^{210}Pb in excess (plotted on a natural logarithmic scale) in the 11 sediment cores. The dotted lines show the linear fit in the upper section of the cores (blue circles) associated with the ^{210}Pb$_{ex}$ flux to the water-sediment interface. The orange squares represent ^{210}Pb in excess in the bottom section, which is not explained by this source. The horizontal gray zones represent the limit in oxic conditions in cores E33, B11, B18, B8E21 and B8E36. For the other cores these limits were founded deeper (see Fig. 4). (For interpretation of the references to color in this figure legend, the reader is referred to the Web version of this article.)

ranged from 53 to 561 Bq·m^2·yr^{-1}. Lower ^{210}Pb fluxes were calculated for cores in the abyssal area, and higher ^{210}Pb fluxes in the continental shelf. The continental slope cores (F38, TS1 and B11) show relatively high ^{210}Pb fluxes. In general, the mixing parameters in the upper sections of the cores, based on ^{210}Pb profiles, were comparable to those reported previously for the region (Díaz-Asencio et al., 2020). Furthermore, we calculated the total unsupported ^{210}Pb inventory in each sediment core to evaluate the effect of other sources of ^{210}Pb in excess, different than the flux from the water column (see Table 1).

3.4. Numerical simulation of Pu profiles

Plutonium activity concentrations, inventories and isotope ratios in sediments from the sGM were published elsewhere (Corcho-Alvarado et al., 2022). $^{239+240}$Pu activity profiles showed a maximum in the upper 2 cm layer, and then either a quasi-exponential decrease or no variation with depth. The $^{239+240}$Pu signal penetrated down to 8 to 10 cm depth in the cores, deeper than it would be expected from the low sedimentation rates of a few cm per kyr previously reported for the region (Díaz-Asencio et al., 2020). In each core, there was very little variability

in $^{240}Pu/^{239}Pu$ isotope ratios with depth, with mean values of 0.10 ± 0.01 (core TS1 at 2417 m depth), 0.11 ± 0.01 (core F38 at 2822 m depth), 0.14 ± 0.02 (core A10 at 3340 m depth) and 0.10 ± 0.01 (core C23 at 3739 m depth) in deep-sea sediment cores. In the outer shelf cores, the mean isotope ratio was slightly higher with mean values of 0.17 ± 0.01 (B8E21 at 419 m) and 0.16 ± 0.01(B8E36 at 257 m).

The $^{239+240}Pu$ profiles and the biodiffusion and sedimentation parameters were modeled with a finite differential solution of the advection-diffusion equation (10). We assumed that $^{239+240}Pu$ entered the sediment as a single pulse in 1960. The model output was fitted to the $^{239,240}Pu$ depth profiles measured in each core, from which the parameters D_{b1}, D_{b2} and S_m" were estimated (Table 2). The best model fits for each core are shown in Fig. 6. For sediment cores B8E36, B8E21, F38, and A10, the model closely reproduced the measured data (R^2 = 0.86–0.98). In contrast, for cores TS1 (R^2 = 0.63) and C23 (R^2 = 0.40), subsurface peaks at 2.5 cm and 6.3 cm, respectively, deviated from the expected model behavior.

The S_m and S_m" values obtained from both ^{14}C dating and $^{239+240}Pu$ modeling, respectively were comparable and remained below 15 cm kyr^{-1} in all sites, except in B8E36 where ^{14}C derived value was too high. The short biodiffusion coefficients obtained from $^{234}Th_{ex}$ decay ($D_{b\text{-}Th}$) were lower than 800 cm^2 kyr^{-1}, showing high variability among sites and were higher than the values estimated from the short mixing parameters from the Pu simulation (D_{b1}). The corresponding coefficients for ^{210}Pb ($D_{b\text{-}Pb}$) were lower than 200 cm^2 kyr^{-1} at all sites, except in core B8E36. At slope and abyssal sites, $D_{b\text{-}Pb}$ and the $^{239+240}Pu$ -derived coefficient (D_{b2}) were more similar.

4. Discussion

4.1. Biodiffusion in the surface mixing layer

The short-term biodiffusion coefficients ($D_{b\text{-}Th}$), obtained from $^{234}Th_{ex}$, were lower than 830 cm^2 kyr^{-1}, except in core E33 (4.14 cm^2 yr^{-1}). These short-term biodiffusion values are higher than the long-term biodiffusion obtained from $^{210}Pb_{ex}$. However, our values of short-term biodiffusion are significantly lower than the value 60 cm^2 yr^{-1} reported for Santa Catalina Basin, California (Smith et al., 1993) and for the mean value of 25 cm^2 yr^{-1} reported in the shelf/slope sediment off Cape Hatteras, North Carolina (Green et al., 2002), both regions characterized by higher export from primary productivity to the sediments and higher abundances and diversity of benthic fauna. The range of mixing depths derived from $^{234}Th_{ex}$ (between 0.3 and 2.9 cm) was similar to the values reported by Yeager et al. (2004) for the Northern Gulf of Mexico (0.5 to 4.0 cm). However, Yeager et al. (2004) reported a $D_{b\text{-}Th}$ range varying from 2000 to 30000 cm^2 kyr^{-1}, much higher than our estimation probably associated with the Mississippi river discharges.

The $^{210}Pb_{ex}$ profiles in the upper section (3-10 cm) of the sediment cores from the slope and abyssal regions exhibit an exponential decay pattern ($R^2 > 0.7$). Furthermore, the $^{234}Th_{ex}$ profiles also had a good exponential fit in the first cm. These results confirm that biodiffusion processes dominate the mixing process in surface sediments in the study areas.

The long-term biodiffusion coefficients obtained using ^{210}Pb ($D_{b\text{-}Pb}$ range from 54 to 549 cm^2 kyr^{-1}) are comparable to those reported previously for the sGM (Díaz-Asencio et al., 2020), but lower than those

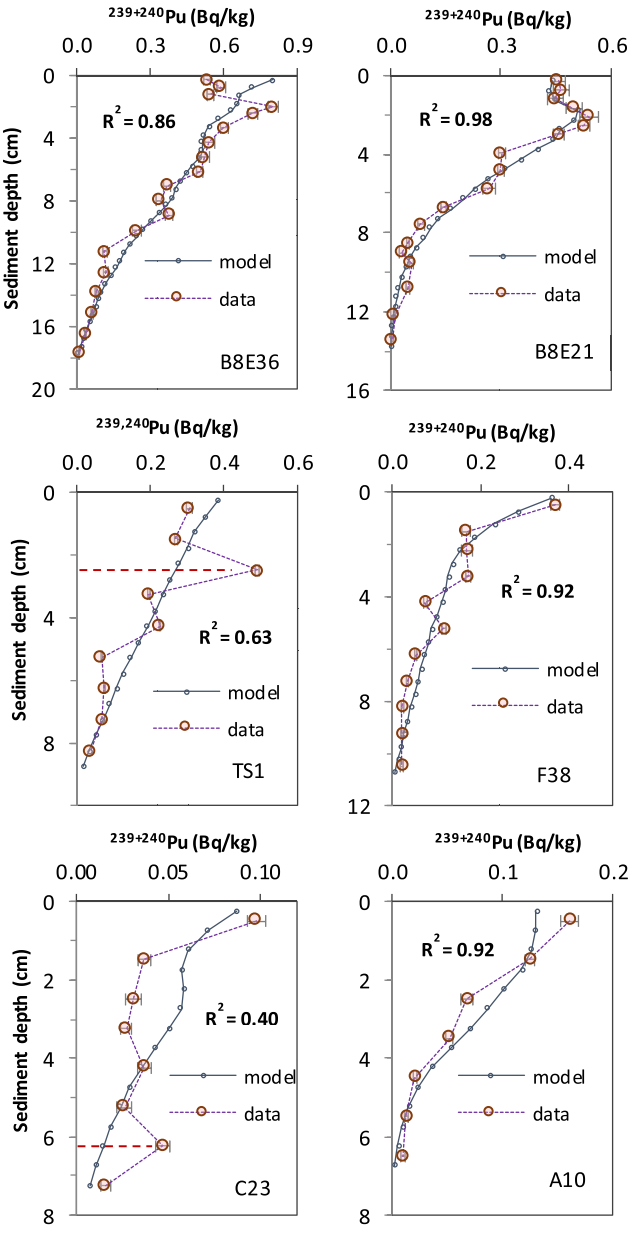

Fig. 6. Depth profiles of the analyzed activity of $^{239,240}Pu$ (Corcho-Alvarado et al., 2022) and the values obtained from the numerical simulation in six sediment cores. The horizontal bars represent the uncertainties estimated at a 68% confidence level.

Table 2
Sedimentation rates, short- and long-term biodiffusion coefficients obtained from ^{14}C, $^{234}Th_{ex}$ and $^{210}Pb_{ex}$, and results of the numerical simulation of Pu profiles sGM.

Station	Water Depth	^{14}C dating and biodiffusion models ($^{210}Pb_{ex}$ and $^{234}Th_{ex}$)			Pu numerical simulation			
	m	$S_{m\ C\text{-}14}$ cm kyr^{-1}	$D_{b\text{-}Th}$ $cm^2 \cdot kyr^{-1}$	$D_{b\text{-}Pb}$ $cm^2 \cdot kyr^{-1}$	S_m" cm·kyr^{-1}	D_{b1}' cm^2 kyr^{-1}	D_{b2}' cm^2 kyr^{-1}	R^2
B8E36	257	34	628	549	12	300	200	0.86
B8E21	419	15	443	206	10	133	64	0.98
TS1	2417	13	832	159	13	800	178	0.57
F38	2822	12	418	164	12	250	200	0.92
C23	3739	9	810	77	8	100	50	0.40
A10	3340	0	95	54	1	30	20	0.92

reported for the nGM (200 to 6000 cm^2 kyr^{-1}; Santschi and Rowe, 2008). In our study, the mixing depths ranged from 5 to 18 cm (Table 1), close to the maximum mixing depth of 14 cm previously reported in these areas of the sGM (Díaz-Asencio et al., 2020). Previous reports on homogeneity of the mixed layer in deep-sea sediments (Boudreau, 1986) differ from the variability observed in this study. The lower mixing parameters were obtained in core E33, where the redox boundary was found at 10 cm below the water-sediment interface (Fig. 4 I i). Suboxic to anoxic conditions below 10 cm likely suppress biological activity within the sediments potentially accounting for the observed reduced mixing. In core A10, the accumulation and mixing parameters were very low, suggesting the presence of carbonate dissolution, as observed from the major element profiles (Fig. 4 I a) and the observed sediment deposition hiatus at least for the past 4 kyr (Díaz-Asencio et al., 2020).

In the two continental shelf cores (B8E36 and B8E21) the $D_{b\text{-}Pb}$ and mixing depths were higher than the values from the abyssal plain and continental slope regions (see Table 1). The values of $D_{b\text{-}Pb}$ in these cores (549 and 206 cm^2 kyr^{-1}) were close to the range reported shallower than the 500 m depth (from 300 to 2000 cm^2 kyr^{-1}) in the upper continental slope near Cape Hatteras, North Carolina, US (Alperin et al., 2002).

The biodiffusion coefficients $D_{b\text{-}Th}$ and $D_{b\text{-}Pb}$ show no relationship with water depths. In all cores, the short-term coefficient ($D_{b\ Th}$) is higher than the long-term coefficient ($D_{b\text{-}Pb}$), although the difference is less than one order of magnitude, in contrast to the two orders of magnitude reported for other deep-sea sites (Smith et al., 1993). These results may be explained by the fact that the intensity of bioturbation processes in marine sediments is proportional to the input of organic matter from the water column (Johnson et al., 2007; Smith and Rabouille, 2002b; Trauthl et al., 1997). These results support the notion that the oligotrophic condition of the water column in the sGM (Linacre et al., 2015) limit the input of organic matter to the sediments, thereby reducing bioturbation and, consequently, the vertical penetration of radionuclides (as well as other particle tracers) from the water-sediment interface.

4.2. ^{210}Pb accumulation and recent diagenesis in bottom sediments

We observe a good relationship between the fluxes of $^{234}Th_{ex}$ and $^{210}Pb_{ex}$ from the water column to the water-sediment interface (Fig. 7a), suggesting that both radionuclides are in steady-state in the water column. However, we have found notable differences between the inventories of unsupported ^{210}Pb from the water column to the water-sediment interface and the inventories of excess ^{210}Pb at depth in the sediment cores (Fig. 7b). Differences between both ^{210}Pb inventories are not observed in stations from the continental shelves, where a change in redox conditions occurs in the first 2 cm of sediments (Fig. 4 II j,k).

This result is consistent with the existence of at least two sources of ^{210}Pb in the sediments: i) the first one from the water column, and ii) the second one associated with the remobilization of ^{226}Ra in sediments under suboxic to anoxic conditions and its reprecipitation, with MnO_2, in sediments with oxic conditions. Thus, Mn redox cycling may act as a trap for Ra. The ^{226}Ra accumulated in oxic layers would produce an upward flux of ^{222}Rn by diffusion, which would explain the observed increase in the excess of ^{210}Pb in the upper layers.

In the stations of the continental shelf (B8E21 and B8E36), ^{222}Rn has most likely seeped out completely from the sediments to the water column. The excess of ^{222}Rn in bottom waters then would increase the flux of ^{210}Pb to the water-sediment interface during the setting of particulate matters. This process may also explain the higher flux of ^{210}Pb to the water-sediment interface in these stations, as well as the higher fluxes of ^{210}Pb previously reported in deep areas of the northern GM ((Santschi and Rowe, 2008) and in slopes of north GM (Schwing et al., 2017).

The non-exponential decrease of excess ^{210}Pb in sediment cores from the slope and abyssal regions -where an exponential decline is typically

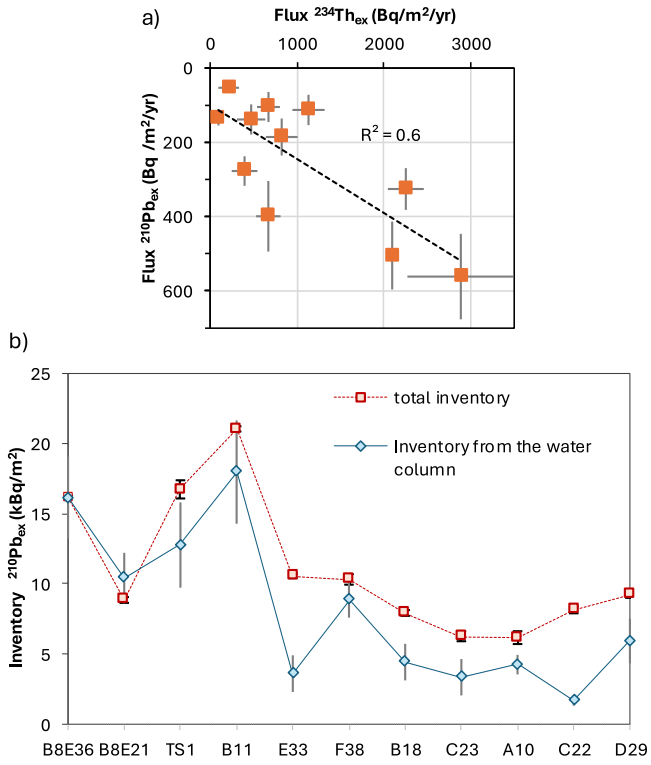

Fig. 7. a) Comparison of the $^{234}Th_{ex}$ and $^{210}Pb_{ex}$ fluxes to the water-sediment interface. The horizontal and vertical bars represent uncertainties estimated at a 68% confidence level. b) $^{210}Pb_{ex}$ inventory to the water-sediment interface (from water column) vs all ^{210}Pb inventory in the sediment cores. The horizontal bars represent the uncertainties estimated at a 68% confidence level.

expected-may be explained by the mobilization of ^{226}Ra under suboxic condition, as inferred from Mn/Al enriched layers, and its subsequent diffusion toward the upper sediment layers. This reprecipitation of ^{226}Ra, associated with MnO_2, acts as an autochthonous source of $^{210}Pb_{ex}$ in the sediment layers, a process that would also explain the non-equilibrium state observed between ^{214}Pb and ^{210}Pb in the deeper layers of several sediment cores. These findings contribute to a better understanding of the specific conditions previously reported in deep regions of the Gulf of Mexico (Díaz-Asencio et al., 2020; Watson and Angino, 1969), associated with the mobilization and reprecipitation of 226Ra, primarily controlled by Mn redox cycling.

Furthermore, this process has also been reported in sediments from the abyssal zones of the Pacific and Atlantic oceans (Kadko, 1980; Lin et al., 2024; Sarmiento et al., 1978; Sarmiento and Broecker, 1980; Suckow et al., 2001). In any case, in future field campaigns, it would be important to determine ^{222}Rn and ^{226}Ra levels in bottom waters and sediment pore waters to further verify these results and the diagenetic processes discussed here.

4.3. Evaluation of sediment accumulation and biodiffusion coefficients in recent sediments

The mean sediment accumulation rates (S_m and S_m") calculated using both ^{14}C dating and $^{239+240}$Pu simulation were comparable and varied between 1 and 15 cm kyr^{-1} (Fig. 8a), except in B8E36, where the ^{14}C derived value was much higher (34 cm kyr^{-1}). These S_m values are in the range previously reported for the Gulf of Mexico (Díaz-Asencio et al., 2020; Santschi and Rowe, 2008; Watson and Angino, 1969), but higher than those reported for oceanic abyssal plains (Kershaw, 1985). The consistency of mean sediment accumulation rates derived from $^{239+240}$Pu and ^{14}C -despite their different half-lives, sources, and

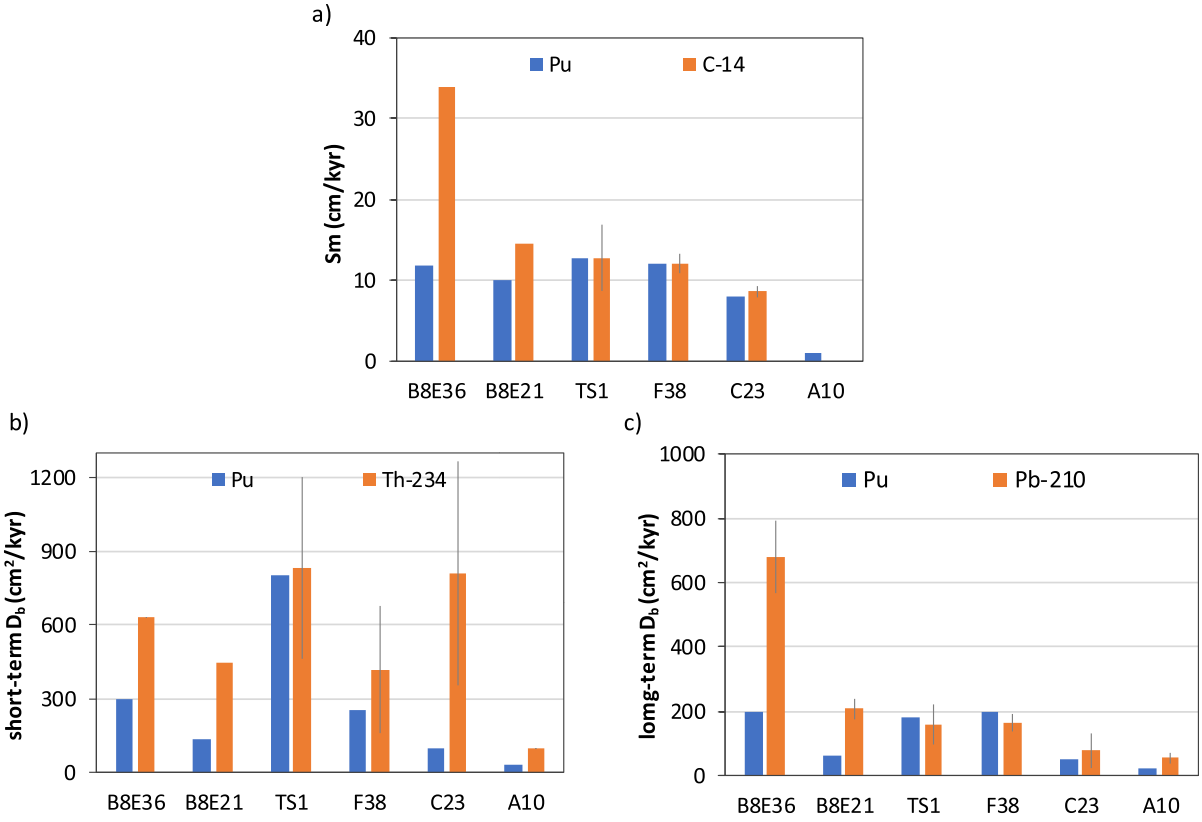

Fig. 8. Comparison of: a) mean sedimentation accumulation rates from Pu numerical simulation vs ^{14}C dating in planktonic foraminifera; b) the short-term biodiffusion coefficients obtained from Pu numerical simulation vs the ^{234}Th in excess profiles; and c) the long-term biodiffusion coefficients obtained from Pu numerical simulation vs the ^{210}Pb in excess profiles. In all cases, horizontal bars represent the uncertainties estimated at a 68% confidence level.

biogeochemical behaviors-demonstrates their reliability for assessing sedimentation across marine settings, from the continental shelf to the abyssal zones.

The short-term biodiffusion coefficients estimated from $^{234}Th_{ex}$ profiles ($D_{b\text{-}Th}$) showed significant differences between cores, as well as high variability compared to the values of D_{b1} obtained from $^{239+240}Pu$ simulations (Fig. 8b). In fact, due to its short half-life, biodiffusion inferred from ^{234}Th provides a better representation of mixing processes on short timescales (<100 days) than $^{239+240}Pu$.

The long-term biodiffusion coefficients were lower than 200 cm^2 kyr^{-1} in all cores, except in B8E36 (549 cm^2 kyr^{-1}, from ^{210}Pb profile estimation). The values for both tracer methods (^{210}Pb and $^{239+240}Pu$) were comparable in all sediment cores, except in B8E36 (Fig. 8c and Table 2). However, the values estimated for the biodiffusion rates with ^{210}Pb ($D_{b\text{-}Pb}$) were higher than Pu estimation in most sites. We have already shown that Pu radionuclide penetration in deep marine sediments is primarily driven by bioturbation rather than accumulation processes.

These findings indicate that modeling of $^{239+240}Pu$ distribution in sediment cores through an advection-diffusion framework provides a robust method for estimating sedimentary parameters such as biodiffusion and accumulation rates. The results are consistent with those derived from the ^{210}Pb and ^{14}C tracers, reinforcing the reliability of this approach.

5. Conclusion

The short-term biodiffusion coefficient $D_{b\text{-}Th}$ (100 d time scale) values were less than one order of magnitude higher than the long-term $D_{b\text{-}Pb}$ (100 yr time scale), in contrast to the two orders of magnitude difference between $D_{b\text{-}Th}$ and $D_{b\text{-}Pb}$ reported in deep ocean sites. The sediment mixing patterns in the investigated sites are linked to the oligotrophic condition of the water column in the southern Gulf of Mexico. The low nutrient input into the mixed layer of the sGM and its consequently low export to the sediment limits the abundance of benthic organisms on the sea floor and to the bioturbation processes and, thus, the vertical penetration of radionuclides (and other particle tracers) from the sediment-water interface down the sediment column.

At all sediment cores, the fluxes of $^{234}Th_{ex}$ and $^{210}Pb_{ex}$ from the water column to the water-sediment interface showed a good relationship, suggesting a steady-state equilibrium of these radionuclides and their parents in the water column. The $^{210}Pb_{ex}$ fluxes from the water column to the sediments are the main source of non-supported ^{210}Pb. However, in the sediment cores from slope and abyssal regions, there is a secondary source of ^{210}Pb which is associated with the remobilization of sedimentary ^{226}Ra under suboxic conditions and its reprecipitation in the oxic layers. This diagenetic process modifies the supported and excess ^{210}Pb profiles, and therefore its application in the evaluation of sediment accumulation or biodiffusion rates.

The identification and extent of this process (mobilization–reprecipitation of ^{226}Ra) were inferred from Mn/Al-enriched layers, suggesting a control by Mn redox cycling. The diffusion of ^{226}Ra to the upper sections of the sediment column may explain the additional concentrations above the expected exponential decrease of excess ^{210}Pb observed in sediment cores from the slopes and abyssal zones. This autochthonous source of $^{210}Pb_{ex}$ within the sediment layers also explains the non-equilibrium state observed between ^{214}Pb and ^{210}Pb at the bottom layers of some cores. Our results could help to elucidate conditions reported previously in deep and slope zones in the Gulf of Mexico.

In the six sediment cores for where the $^{239+240}Pu$ profiles were compared with the numerical model solution, the profiles fit well, with

$R^2 > 0.86$ in four of the six cores. The set of sedimentary parameters (D_{b1}', D_{b2}', and S_m') estimated from $^{239+240}$Pu simulation were comparable to those obtained with the tracers ^{234}Th, ^{210}Pb and ^{14}C. The $^{239+240}$Pu deconvolution showed high differences with ^{234}Th profiles most likely due to the short time scale nature of the mixing processes (<100 days). Our results demonstrated that sedimentary parameters derived from $^{239+240}$Pu data are suitable for evaluating short-term scale processes (<100 d). The biodiffusion rates estimated from $^{239+240}$Pu are comparable to those obtained from ^{210}Pb profiles (long-term scale), although the values from ^{210}Pb are slightly higher in four of the six cases. The accumulation rates estimated from $^{239+240}$Pu data were also comparable to those obtained from the ^{14}C dating approach, except for core B8E36.

The results have significant implications for understanding and evaluating different processes in deep-sea sediments, including bioturbation and sediment accumulation, early diagenesis and Ra remobilization, as well as the fluxes, degradation, and burial of organic carbon. These processes may be influenced under the current context of global climate change.

CRediT authorship contribution statement

M. Díaz-Asencio: Writing – review & editing, Writing – original draft, Visualization, Validation, Supervision, Methodology, Investigation, Formal analysis, Data curation, Conceptualization. **J.A. Corcho-Alvarado:** Writing – review & editing, Writing – original draft, Validation, Methodology, Formal analysis, Data curation, Conceptualization. **O. Díaz-García:** Writing – review & editing, Writing – original draft, Visualization, Software, Methodology, Data curation, Conceptualization. **J.C. Herguera:** Writing – review & editing, Writing – original draft, Visualization, Project administration, Methodology, Investigation, Data curation, Conceptualization. **M.A. Huerta-Diaz:** Writing – review & editing, Writing – original draft, Methodology, Formal analysis, Data curation. **P.T. Schwing:** Writing – review & editing, Writing – original draft, Methodology, Formal analysis, Data curation. **R. Larson:** Writing – review & editing, Writing – original draft, Methodology, Formal analysis, Data curation. **G.R. Brook:** Writing – review & editing, Writing – original draft, Methodology, Formal analysis, Data curation. **S. Röllin:** Writing – review & editing, Methodology, Formal analysis, Data curation. **L.W. Daessle:** Writing – review & editing, Methodology, Formal analysis, Data curation.

Declaration of competing interest

The authors declare that they have no known competing financial interests or personal relationships that could have appeared to influence the work reported in this paper.

Acknowledgments

This study is a contribution of Project No 201441 "Implementation of oceanographic observation networks (physical, geochemical, ecological) for the generation of scenarios in the case of possible contingencies related to the exploration and production of hydrocarbons in deep waters of the Gulf of Mexico," funded by the Hydrocarbon fund SENER-CONACyT. This is a contribution of the Gulf of Mexico Research Consortium (CIGoM).

This study was also suport for the Research Contract # 23493 “Radionuclides and Stable Isotopic determinations to understand the Organic Matter Cycle in sediments of Marine Ecosystems of the southern Gulf of Mexico” supported for the Coordinate Research Program K41019 “Applied Radioecological Tracers to Assess Coastal and Marine Ecosystem Health” from the IAEA Technical Cooperation Program.

We would like to express our sincere gratitude to the two anonymous reviewers for their detailed reviews, as well as for their valuable observations and constructive suggestions, which have significantly improved the quality and clarity of this manuscript. We also thank the editor for their guidance throughout the review process.

Appendix A. Supplementary data

In the Supplementary Data, we present concentrations of Al, Fe, and Mn, along with activities of excess 234Th, 210Pb, and 214Pb in all sediment cores. Additionally, we include the animation of Pu accumulation in sediments from 1962 to 2021 across the six analysed sediment cores. The Supplementary Data to this article can be found online at https://doi.org/10.1016/j.jenvrad.2026.107980.

Data availability

The data could be made available in the supplementary tables.

References

Alperin, M.J., Suayah, I.B., Benninger, L.K., Martens, C.S., 2002. Modern organic carbon burial fluxes, recent sedimentation rates, and particle mixing rates from the upper continental slope near Cape Hatteras, North Carolina (USA). Deep Sea Res. Part II Top. Stud. Oceanogr. 49, 4645–4665. https://doi.org/10.1016/S0967-0645(02)00133-9.

Anderson, R.F., Bopp, R.F., Buesseler, K.O., Biscaye, P.E., 1988. Mixing of particles and organic constituents in sediments from the continental shelf and slope off Cape Cod: SEEP—I results. Cont. Shelf Res. 8, 925–946. https://doi.org/10.1016/0278-4343(88)90082-9.

Appleby, P.G., Oldfield, F., 1978. The calculation of lead-210 dates assuming a constant rate of supply of unsupported 210Pb to the sediment. Catena (Amst). 5, 1–8. https://doi.org/10.1016/S0341-8162(78)80002-2.

Athié, G., Sheinbaum, J., Candela, J., Ochoa, J., Pérez-Brunius, P., Romero-Arteaga, A., 2020. Seasonal variability of the transport through the Yucatan channel from observations. J. Phys. Oceanogr. 50, 343–360. https://doi.org/10.1175/JPO-D-18-0269.1.

Athié, G., Sheinbaum, J., Leben, R., Ochoa, J., Shannon, M.R., Candela, J., 2015. Interannual variability in the Yucatan Channel flow. Geophys. Res. Lett. 42, 1496–1503. https://doi.org/10.1002/2014GL062674.

Benninger, L.K., Aller, R.C., Cochran, J.K., Turekian, K.K., 1979. Effects of biological sediment mixing on the210Pb chronology and trace metal distribution in a Long Island Sound sediment core. Earth Planet Sci. Lett. 43, 241–259. https://doi.org/10.1016/0012-821X(79)90208-5.

Boudreau, B.P., 1986. Mathematics of tracer mixing in sediments; I, spatially-dependent, diffusive mixing. Am. J. Sci. 286, 161–198. https://doi.org/10.2475/ajs.286.3.161.

Brooks, G.R., Larson, R.A., Devine, B., Schwing, P.T., 2015a. Annual to millennial record of sediment delivery to US Virgin Island coastal environments. Holocene 25, 1015–1026. https://doi.org/10.1177/0959683615575357.

Brooks, G.R., Larson, R.A., Schwing, P.T., Romero, I., Moore, C., Reichart, G.J., Jilbert, T., Chanton, J.P., Hastings, D.W., Overholt, W.A., Marks, K.P., Kostka, J.E., Holmes, C.W., Hollander, D., 2015b. Sedimentation pulse in the NE Gulf of Mexico following the 2010 DWH blowout. PLoS One. https://doi.org/10.1371/journal.pone.0132341.

Buesseler, K.O., Sholkovitz, E.R., 1987a. The geochemistry of fallout plutonium in the North Atlantic: I. A pore water study in shelf, slope and deep-sea sediments. Geochem. Cosmochim. Acta 51, 2605–2622. https://doi.org/10.1016/0016-7037(87)90143-8.

Buesseler, K.O., Sholkovitz, E.R., 1987b. The geochemistry of fallout plutonium in the North Atlantic: II. ratios and their significance. Geochem. Cosmochim. Acta 51, 2623–2637. https://doi.org/10.1016/0016-7037(87)90144-X.

Carvalho, F.P., Oliveira, J.M., Soares, A.M.M., 2011. Sediment accumulation and bioturbation rates in the deep Northeast Atlantic determined by radiometric techniques. ICES (Int. Counc. Explor. Sea) J. Mar. Sci. 68, 427–435. https://doi.org/10.1093/icesjms/fsr005.

Corcho-Alvarado, J.A., Díaz-Asencio, M., Röllin, S., Herguera, J.C., 2022. Distribution and source of plutonium in sediments from the southern Gulf of Mexico. Environ. Sci. Pollut. Control Ser. 29, 85766–85776. https://doi.org/10.1007/s11356-022-18770-6.

DeMaster, D.J., Cochran, J.K., 1982. Particle mixing rates in deep-sea sediments determined from excess 210Pb and 32Si profiles. Earth Planet Sci. Lett. 61, 257–271. https://doi.org/10.1016/0012-821X(82)90057-7.

Díaz-Asencio, M., Bartrina, V.F., Herguera, J.C., 2019. Sediment accumulation patterns on the slopes and abyssal plain of the southern Gulf of Mexico. Deep Sea Res. Oceanogr. Res. Pap. https://doi.org/10.1016/J.DSR.2019.01.003.

Díaz-Asencio, M., Herguera, J.C., Romero, F.G., Rafter, P., 2023. Sediment accumulation rates and carbonate fluxes of deep-sea sediments in the southern Gulf of Mexico. Mar. Geol. 464. https://doi.org/10.1016/j.margeo.2023.107131.

Díaz-Asencio, M., Herguera, J.C., Schwing, P.T., Larson, R.A., Brooks, G.R., Southon, J., Rafter, P., 2020. Sediment accumulation rates and vertical mixing of deep-sea sediments derived from14C and 210Pb in the southern Gulf of Mexico. Mar. Geol. 429, 106288. https://doi.org/10.1016/j.margeo.2020.106288.

Erlenkeuser, H., 1980. 14C age and vertical mixing of deep-sea sediments. Earth Planet Sci. Lett. https://doi.org/10.1016/0012-821X(80)90018-7.

Froelich, P.N., Klinkhammer, G.P., Bender, M.L., Luedtke, N.A., Heath, G.R., Cullen, D., Dauphin, P., Hammond, D., Hartman, B., Maynard, V., 1979. Early oxidation of organic matter in pelagic sediments of the eastern equatorial Atlantic: suboxic diagenesis. Geochem. Cosmochim. Acta 43, 1075–1090. https://doi.org/10.1016/0016-7037(79)90095-4.

Green, M.A., Aller, R.C., Cochran, J.K., Lee, C., Aller, J.Y., 2002. Bioturbation in shelf/slope sediments off Cape Hatteras, North Carolina: the use of 234Th, Chl-a, and Br− to evaluate rates of particle and solute transport. Deep Sea Res. Part II Top. Stud. Oceanogr. 49, 4627–4644. https://doi.org/10.1016/S0967-0645(02)00132-7.

Guinasso, N.L., Schink, D.R., 1975. Quantitative estimates of biological mixing rates in abyssal sediments. J. Geophys. Res. 80, 3032–3043. https://doi.org/10.1029/JC080i021p03032.

Henderson, G.M., Lindsay, F.N., Slowey, N.C., 1999. Variation in bioturbation with water depth on marine slopes: a study on the Little Bahamas Bank. Mar. Geol. 160, 105–118. https://doi.org/10.1016/S0025-3227(99)00018-3.

Holmes, C.W., 1976. DISTRIBUTION, regional variation, and geochemical coherence of selected elements in the sediments of the central gulf of Mexico. U. S. Geol. Surv. Prof. Pap. https://doi.org/10.3133/pp928.

Johnson, N.A., Campbell, J.W., Moore, T.S., Rex, M.A., Etter, R.J., McClain, C.R., Dowell, M.D., 2007. The relationship between the standing stock of deep-sea macrobenthos and surface production in the western North Atlantic. Deep. Sea. Res. 1. Oceanogr. Res. Pap. https://doi.org/10.1016/j.dsr.2007.04.011.

Kadko, D., 1980. 230Th,226Ra and222Rn in abyssal sediments. Earth Planet Sci. Lett. 49, 360–380. https://doi.org/10.1016/0012-821X(80)90079-5.

Kershaw, P.J., 1985. 14C and 210Pb in NE atlantic sediments: evidence of biological reworking in the context of radioactive waste disposal. J. Environ. Radioact. 2, 115–134. https://doi.org/10.1016/0265-931X(85)90002-5.

Kirk Cochran, J., Kadko, D.C., 2008. Chapter 10 Uranium- and thorium-series radionuclides. In: Marine Groundwaters, pp. 345–382. https://doi.org/10.1016/S1569-4860(07)00010-1.

Koide, M., Soutar, A., Goldberg, E.D., 1972. Marine geochronology with210Pb. Earth Planet Sci. Lett. 14, 442–446. https://doi.org/10.1016/0012-821X(72)90146-X.

Larson, R.A., Brooks, G.R., Schwing, P.T., Holmes, C.W., Carter, S.R., Hollander, D.J., 2018a. High-resolution investigation of event driven sedimentation: northeastern Gulf of Mexico. Anthropocene 24, 40–50. https://doi.org/10.1016/j.ancene.2018.11.002.

Larson, R.A., Brooks, G.R., Schwing, P.T., Holmes, C.W., Carter, S.R., Hollander, D.J., 2018b. High-resolution investigation of event driven sedimentation: northeastern Gulf of Mexico. Anthropocene 24, 40–50. https://doi.org/10.1016/j.ancene.2018.11.002.

Leben, R.R., 2013. Altimeter-Derived loop Current metrics. https://doi.org/10.1029/161GM15.

Legeleux, F., Reyss, J.-L., Schmidt, S., 1994. Particle mixing rates in sediments of the northeast tropical Atlantic: evidence from 210Pbxs, 137Cs, 228Thxs and 234Thxs downcore distributions. Earth Planet Sci. Lett. 128, 545–562. https://doi.org/10.1016/0012-821X(94)90169-4.

Lin, F., Lin, C., Sun, X., Lin, H., Lin, L., Deng, F., Tan, K., Lin, P., 2024. Bioturbation coefficients and organic carbon degradation rates of deep-sea sediments in the central-eastern tropical Pacific. Acta Oceanol. Sin. https://doi.org/10.1007/s13131-024-2413-9.

Linacre, L., Lara-Lara, R., Camacho-Ibar, V., Herguera, J.C., Bazán-Guzmán, C., Ferreira-Bartrina, V., 2015. Distribution pattern of picoplankton carbon biomass linked to mesoscale dynamics in the southern gulf of Mexico during winter conditions. Deep. Sea. Res. 1. Oceanogr. Res. Pap. https://doi.org/10.1016/j.dsr.2015.09.009.

Mangeret, A., Reyss, J.-L., Seder-Colomina, M., Stetten, L., Morin, G., Thouvenot, A., Souhaut, M., van Beek, P., 2020. Early diagenesis of radium 226 and radium 228 in lacustrine sediments influenced by former mining sites. J. Environ. Radioact. 222, 106324. https://doi.org/10.1016/j.jenvrad.2020.106324.

Mejía-Piña, K.G., Huerta-Diaz, M.A., González-Yajimovich, O., 2016. Calibration of handheld X-ray fluorescence (XRF) equipment for optimum determination of elemental concentrations in sediment samples. Talanta 161, 359–367. https://doi.org/10.1016/j.talanta.2016.08.066.

Meunier, T., Pallás-Sanz, E., Tenreiro, M., Portela, E., Ochoa, J., Ruiz-Angulo, A., Cusí, S., 2018. The vertical structure of a loop current eddy. J. Geophys. Res., Oceans 123, 6070–6090. https://doi.org/10.1029/2018JC013801.

Meunier, T., Sheinbaum, J., Pallàs-Sanz, E., Tenreiro, M., Ochoa, J., Ruiz-Angulo, A., Carton, X., de Marez, C., 2020. Heat content Anomaly and Decay of warm-core rings: the case of the Gulf of Mexico. Geophys. Res. Lett. 47. https://doi.org/10.1029/2019GL085600.

Nozaki, Y., Kirk Cochran, J., Turekian, K.K., Keller, G., 1977. Radiocarbon and 210Pb distribution in submersible-taken deep-sea cores from project FAMOUS. Earth Planet Sci. Lett. 34, 167–173. https://doi.org/10.1016/0012-821X(77)90001-2.

Officer, C.B., 1982. Mixing, sedimentation rates and age dating for sediment cores. Mar. Geol. 46, 261–278. https://doi.org/10.1016/0025-3227(82)90084-6.

Officer, C.B., Lynch, D.R., 1983. Mixing, sedimentation rates and age dating for sediment cores — reply I. Mar. Geol. 52, 292–296. https://doi.org/10.1016/0025-3227(83)90063-4.

Pope, R.H., Demaster, D.J., Smith, C.R., Seltmann, H., 1996. Rapid bioturbation in equatorial Pacific sediments: evidence from excess 234Th measurements. Deep Sea Res. Part II Top. Stud. Oceanogr. 43, 1339–1364. https://doi.org/10.1016/0967-0645(96)00009-4.

Quintanilla, J.G., Herguera, J.C., Sheinbaum, J., 2024. Oxygenation of the Gulf of Mexico thermocline linked to the detachment of Loop Current eddies. Front. Mar. Sci. 11. https://doi.org/10.3389/fmars.2024.1479837.

Robbins, J.A., 1978. Geochemical and geophysical applications of radioactive lead. In: Nriagu, J.O. (Ed.), The Biogeochemistry of Lead in the Environment. Elsevier, Amsterdam, pp. 285–293.

Robbins, J.A., McCall, P.L., Fisher, J.B., Krezoski, J.R., 1979. Effect of deposit feeders on migration of137Cs in lake sediments. Earth Planet Sci. Lett. 42, 277–287. https://doi.org/10.1016/0012-821X(79)90035-9.

Roberts, K.A., Cochran, J.K., Barnes, C., 1997. 210Pb and 239,240Pu in the Northeast Water Polynya, Greenland: particle dynamics and sediment mixing rates. J. Mar. Syst. 10, 401–413. https://doi.org/10.1016/S0924-7963(96)00061-9.

Röllin, S., Sahli, H., Holzer, R., Astner, M., Burger, M., 2009. PU and NP analysis of soil and sediment samples with ICP-MS. Appl. Radiat. Isot. https://doi.org/10.1016/j.apradiso.2009.01.041.

Sahli, H., Röllin, S., Putyrskaya, V., Klemt, E., Balsiger, B., Burger, M., Corcho Alvarado, J.A., 2017. A procedure for the sequential determination of radionuclides in soil and sediment samples. J. Radioanal. Nucl. Chem. 314, 2209–2218. https://doi.org/10.1007/s10967-017-5621-3.

Santschi, P.H., Rowe, G.T., 2008. Radiocarbon-derived sedimentation rates in the Gulf of Mexico. Deep Sea Res. Part II Top. Stud. Oceanogr. 55, 2572–2576. https://doi.org/10.1016/j.dsr2.2008.07.005.

Sarmiento, J.L., Broecker, W.S., 1980. OCEAN FLOOR 222Rn STANDING CROPS IN THE ATLANTIC AND PACIFIC OCEANS. Earth Planet Sci. Lett. 49, 341–350.

Sarmiento, J.L., Broecker, W.S., Biscaye, P.E., 1978. Excess bottom radon 222 distribution in deep ocean passages. J. Geophys. Res. 83, 5068. https://doi.org/10.1029/JC083iC10p05068.

Sarmiento, J.L., Gruber, N., 2005. Remineralization and burial in the sediments. In: OCEAN BIOGEOCHEMICAL DYNAMICS. Princeton University Press, New Jersey, pp. 227–266.

Schwing, P.T., Brooks, G.R., Larson, R.A., Holmes, C.W., O'Malley, B.J., Hollander, D.J., 2017. Constraining the spatial extent of marine oil snow sedimentation and flocculent accumulation following the deepwater horizon event using an excess 210 Pb flux approach. Environ. Sci. Technol. 51, 5962–5968. https://doi.org/10.1021/acs.est.7b00450.

Sheinbaum, J., Athié, G., Candela, J., Ochoa, J., Romero-Arteaga, A., 2016. Structure and variability of the Yucatan and loop currents along the slope and shelf break of the Yucatan channel and Campeche bank. Dynam. Atmos. Oceans 76, 217–239. https://doi.org/10.1016/j.dynatmoce.2016.08.001.

Smith, C.R., Pope, R.H., DeMaster, D.J., Magaard, L., 1993. Age-dependent mixing of deep-sea sediments. Geochem. Cosmochim. Acta 57, 1473–1488. https://doi.org/10.1016/0016-7037(93)90007-J.

Smith, C.R., Rabouille, C., 2002a. What controls the mixed-layer depth in deep-sea sediments? The importance of POC flux. Limnol. Oceanogr. https://doi.org/10.4319/lo.2002.47.2.0418.

Smith, C.R., Rabouille, C., 2002b. What controls the mixed-layer depth in deep-sea sediments? The importance of POC flux. Limnol. Oceanogr. 47, 418–426. https://doi.org/10.4319/lo.2002.47.2.0418.

Stordal, M.C., Johnson, J.W., Guinasso, N.L., Schink, D.R., 1985. Quantitative evaluation of bioturbation rates in deep ocean sediments. II. Comparison of rates determined by 210Pb and 239,240Pu. Mar. Chem. 17, 99–114. https://doi.org/10.1016/0304-4203(85)90067-2.

Sturges, W., Hoffmann, N.G., Leben, R.R., 2010. A trigger mechanism for loop current ring separations. J. Phys. Oceanogr. 40 (1), 900–913. https://doi.org/10.1175/2009JPO4245.

Suckow, A., Treppke, U., Wiedicke, M.H., Weber, M.E., 2001. Bioturbation coefficients of deep-sea sediments from the Peru Basin determined by gamma spectrometry of 210Pbexc. Deep Sea Res. Part II Top. Stud. Oceanogr. 48, 3569–3592. https://doi.org/10.1016/S0967-0645(01)00057-1.

Trauthl, M.H., Sarnthein, M., Arnold, M., 1997. Bioturbational mixing depth and carbon flux at the seafloor. Paleoceanography. https://doi.org/10.1029/97PA00722.

Watson, J.A., Angino, E.E., 1969. IRON-RICH layers in sediments from the gulf of Mexico. J. Sediment. Petrol. 39, 1412–1419.

Wetzel, A., Kohl, B., 1986. Accumulation rates of Mississippi fan sediments cored during deep Sea drilling Project leg 96. In: Initial Reports of the Deep Sea Drilling Project, vol. 96. U.S. Government Printing Office. https://doi.org/10.2973/dsdp.proc.96.131.1986.

Yeager, K.M., Santschi, P.H., Rowe, G.T., 2004. Sediment accumulation and radionuclide inventories (239,240Pu, 210Pb and 234Th) in the northern Gulf of Mexico, as influenced by organic matter and macrofaunal density. Mar. Chem. 91, 1–14. https://doi.org/10.1016/j.marchem.2004.03.016.

Yu, W., Lin, F., Lin, L., 2023. Bioturbation in sediment cores from the Clarion-Clipperton Zone in the northeast Pacific: evidence from excess 210Pb. Mar. Pollut. Bull. 188, 114635. https://doi.org/10.1016/j.marpolbul.2023.114635.